X-ray spectral measurements for tungsten-anode from 20 to 49 kVp on a digital breast tomosynthesis system

Da Zhang, Xinhua Li, and Bob Liu[a)]
Department of Radiology, Division of Diagnostic Imaging Physics, Massachusetts General Hospital, Boston, Massachusetts 02114

(Received 23 February 2012; revised 19 April 2012; accepted for publication 4 May 2012; published 29 May 2012)

Purpose: This paper presents new spectral measurements of a tungsten-target digital breast tomosynthesis (DBT) system, including spectra of 43–49 kVp.
Methods: Raw x-ray spectra of 20–49 kVp were directly measured from the tube port of a Selenia Dimensions DBT system using a CdTe based spectrometer. Two configurations of collimation were employed: one with two tungsten pinholes of 25 μm and 200 μm diameters, and the other with a single pinhole of 25 μm diameter, for acquiring spectra from the focal spot and from the focal spot as well as its vicinity. Stripping correction was applied to the measured spectra to compensate distortions due to escape events. The measured spectra were compared with the existing mammographic spectra of the TASMIP model in terms of photon fluence per exposure, spectral components, and half-value layer (HVL). HVLs were calculated from the spectra with a numerical filtration of 0.7 mm aluminum and were compared against actual measurements on the DBT system using W/Al (target-filter) combination, without paddle in the beam.
Results: The spectra from the double-pinhole configuration, in which the acceptance aperture pointed right at the focal spot, were harder than the single-pinhole spectra which include both primary and off-focus radiation. HVL calculated from the single-pinhole setup agreed with the measured HVL within 0.04 mm aluminum, while the HVL values from the double-pinhole setup were larger than the single-pinhole HVL by at most 0.1 mm aluminum. The spectra from single-pinhole setup agreed well with the TASMIP mammographic spectra, and are more relevant for clinical purpose.
Conclusions: The spectra data would be useful for future research on DBT system with tungsten targets.
 [http://dx.doi.org/10.1118/1.4719958]

Key words: x-ray spectrum, spectroscopy, digital breast tomosynthesis

I. INTRODUCTION

The knowledge of x-ray spectra is a cornerstone of many medical imaging researches and developments. For breast imaging, spectral data are useful for optimizing imaging techniques,[1–7] evaluating performance of imaging systems and components,[8–10] calculating dose to the breast,[11–16] estimation of breast composition,[17–19] as well as dual energy and contrast enhanced imaging.[20–22] The computer codes by Boone *et al.*[23,24] cover both the mammographic and general x-ray energy range and have served the medical imaging research community for more than a decade.

In traditional mammography, the tube voltage ranges from 18 to 42 kVp. Today, a wider kilovolt peak (kVp) range is used in digital breast tomosynthesis (DBT). For example, Selenia Dimensions (Hologic, Inc., Bedford, MA) systems employ tungsten targets and operate at 20–49 kVp. The TASMIP model of Boone *et al.* in the mammographic energy range[23] covers 20–42 kVp with tungsten-anode, and the model is based on a Eureka tube (model Mam Rad 100, Eureka x-ray Tube). Their TASMIP model in the general x-ray energy range[24,25] covers an energy range of 30–140 kVp, but the spectra were based on a general x-ray tube designed for nonmammographic applications, and the data of 30–49 kVp were extrapolated from the measurements of 50–140 kVp. Considering the possible differences in operating range of kVp anode angle, intrinsic filtration, and composition of the target and anode disk[26] between the existing data[23–25] and a modern DBT system,[27] we believe there is a need to obtain new spectral data.

For the measurements of x-ray spectra in diagnostic imaging, researchers often use high purity germanium (HPGe) detectors[24] and compound semiconductors such as cadmium zinc telluride (CdZnTe)[28,29] and cadmium telluride (CdTe).[30–32] As compared to HPGe detector, which is generally bulky due to the need for liquid nitrogen cryogenic equipment, CdTe and CdZnTe detectors with small thermoelectric cooler are much more compact and practical in clinical environment.[33] Particularly for mammographic spectroscopy, the limited space between the fixed x-ray tube and breast holder makes the compact spectrometers preferable. While CdZnTe spectra are generally distorted by charge trapping and need to be corrected.[28,29] Miyajima[30] showed that the correction for the distortion due to charge trapping is not necessary when using a CdTe detector in diagnostic x-ray spectroscopy. In this study, we conducted x-ray spectral measurements with a CdTe spectrometer on a Selenia Dimensions DBT system. The resultant x-ray spectra of 20–49 kVp, starting from 2.5 keV and with energy bins of 0.5 keV, are shared as supplemental data for the research community.[40]

TABLE I. Details of the detector of the spectrometer.

Material	CdTe
Density	5.85 g/cm^3
Dimension	$3 \times 3 \times 1$ mm^3
Electrode at front	200 nm thick Pt
Electrode at end	1000 nm thick In
Window material	0.1 mm Be
Bias voltage	500 V

II. MATERIALS AND METHODS

II.A. Spectrometer used in this study

We used an integrated x-ray and gamma ray spectrometer (X-123CdTe, Amptek, Bedford, MA) in this study. The spectrometer has a CdTe Schottky diode detector of $3 \times 3 \times 1$ mm^3, which is mounted on a thermoelectric cooler to reduce electronic noise. The spectrometer combines the detector, preamplifier, digital pulse processor, and multichannel analyzer together in one compact package. We used 1024 channels in the data collection and conducted energy calibration with the 13.95 and 59.54 keV peaks of ^{241}Am. The energy resolution of the spectrometer, in terms of the full width half maximum (FWHM) of 14.4-keV ^{57}Co peak, is 530 eV. Table I listed more details of the detector.

II.B. Spectral measurements

We removed the collimation and filter assembly on the tube of a Selenia Dimensions system and measured the raw x-ray spectra which are more flexible to use. Removal of the collimation assembly also eased the positioning of the spectrometer. The spectrometer was placed with its axis perpendicular to the breast support (Fig. 1), and a metal board was inserted between the spectrometer and the breast support to provide extension toward the chest direction and to protect the imaging detector from excessive radiation. We used tungsten pinholes to limit the photon rate impinging onto the detector, to prevent spectral distortion due to pileup.[29,34]

Because pinholes were used to collimate the incident beam, and because the axis of the spectrometer was perpendicular to the detector, the received photon rate was sensitive to the position of the spectrometer on the breast holder. We carefully positioned the spectrometer regarding the direction of the incident x-ray: the spectrometer was aligned to the center of the tube's output window in the left–right direction, with the help of a laser pointer (see the left of Fig. 1). With its position fixed in the L–R direction, the spectrometer was then moved step by step in the anterior-chest direction. The photon rates at different positions in the anterior-chest were compared, and thus, the "sweet spot" at which the highest photon rate was received by the spectrometer could be located. We used this method to align the axis of the spectrometer-pinhole assembly to the central ray.

The x-ray tube is composed by a tungsten focal track[26] on a molybdenum anode disk (Fig. 1). The anode angle is 16°. The kVp accuracy was verified by the vendor to be within 0.5 kVp from the nominal values. We performed two experiments with different configurations of pinhole collimators to examine the spectra measured with different acceptance apertures to the focal spot.

In the first setup, a single pinhole of diameter of 25 μm was placed on top of a brass spacer that separated the pinhole from the input window of the spectrometer. This setup opened a large acceptance aperture that did not restrict the reception of photons from both the focal spot and its vicinity.

In the second setup, two pinholes were used with the brass spacer separating them. The pinhole on top of the spacer had 200 μm diameter, and the one below the spacer had 25 μm diameter. Based on the distances from the focal spot to the first and second pinholes (418 and 456 mm, respectively), the diameter of the acceptance aperture projected onto the

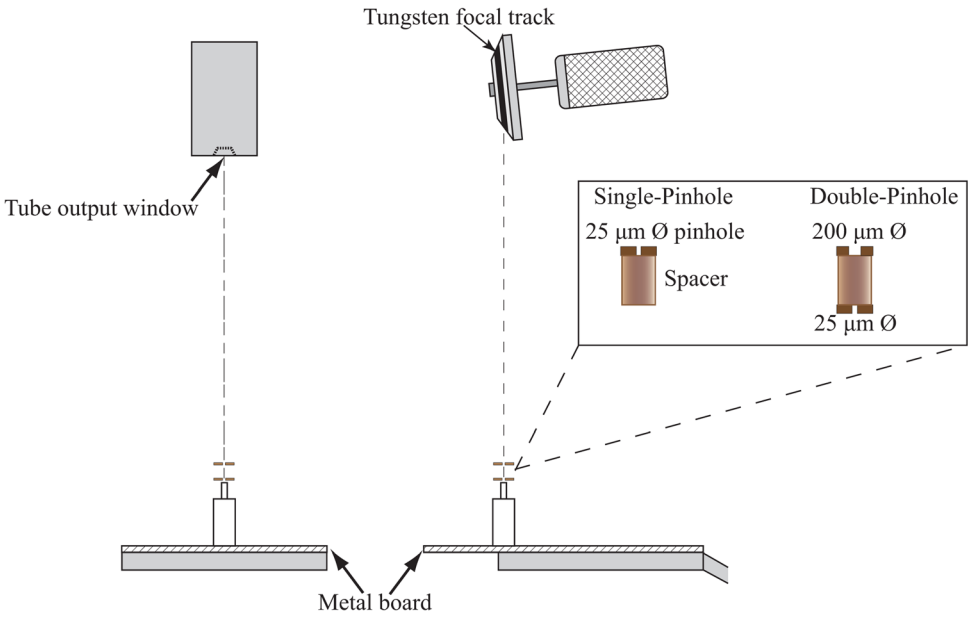

FIG. 1. Experimental setup of the spectral measurements.

(horizontal) plane of the focal spot was approximately 2 mm. The double-pinhole setup was sensitive to its positioning in the anterior-chest direction and moving away from the sweet spot by just 1–2 mm significantly reduced the incident photon rate. The good alignment of the axis of the double-pinhole-spectrometer assembly with the tungsten focal track could minimize the contribution of off-focus x-ray photons from the molybdenum anode disk in the measured spectra.

Since the filter-collimation assembly was removed during the spectral measurements, the raw spectra had much higher photon rate than the spectra filtered by the 0.7 mm aluminum. In this situation, the control of the incident photon rate became an important issue for the spectral measurement. The common approaches of increasing the source to detector distance and making extended exposure with low tube current did not work in this study: the source to image-receptor distance (SID) of the system is fixed as 70 cm, and the tube is designed without fluoroscopic mode and with high exposure rate to alleviate motion artifacts. On the other hand, excessively reducing incident photon rate, for example, by using even smaller pinhole sizes, not only increases the difficulty of alignment but also requires much more repeated exposures to achieve sufficient photon statistics—a heavy burden for the tube. We tackled this difficulty by reducing the tube current to 10–60 mA (depending on kVp) and setting the exposure time at the maximum value of 2.5 s, using a service software from Hologic. In addition, the two configurations of pinholes were carefully chosen to achieve a balance between the incident photon rate and the number of repeated exposures. The dead time of the spectrometer in most of the measurements was around 8%–13% (with the maximum being 15.6%), which was well below the limit level of dead time (30%) recommended by the manufacturer. Four to six repeated exposures were made for each of 20–49 kVp in the double-pinhole setup, depending on the photon rate for the individual spectrum, and the total detected counts ranged from 15.8 to 19.5 K. Three to five repeated exposures were made in the single-pinhole setup for [21, 23, 25,…, 49] as well as 20, 30, and 40 kVp, and the total detected counts ranged from 11.1 to 15.6 K. Due to the concern of damaging the tube, no more repeated exposures were performed.

II.C. Postprocessing of measured spectra

The spectra output from the spectrometer were with 1024 channels covering up to 65 keV, and these raw measurements were rebinned into 0.5-bin-width spectra for the ease of the subsequent steps. The kVp of the raw spectra was determined by a second order polynomial fitting at the tail end of the spectrum, which includes energies up to 1 keV beyond the nominal tube voltage. Counts of channels above the kilovolt (peak) values (due to pile-up), although very insignificant (1–2 per channel if there is any), were removed.

A few potential causes of spectral distortion exist in the spectral measurements with CdTe/CdZnTe detectors: carrier trapping, the transmission (penetrating the detector) of primary x-rays, and the escape of secondary x-rays.[28,30,33] According to the results in Ref. 30, the distortion due to carrier trapping is negligible when a thin CdTe detector is used in the diagnostic x-ray energy range. In traditional mammographic energy range (<35 kVp), the distortion from the escape events are negligible due to the high Z materials of the detector.[29] On the other hand, with the range of kilovolt (peak) spanned to 49 kVp, it is necessary to examine the distortion due to the escape events.

The stripping method was used to correct the measured spectra for the escape events (transmitted primary and escaped secondary x-rays)[28,32,35]

$$N_t(E_0) = \frac{N_d(E_0) - \sum_{E=E_0+0.5}^{E_{\max}} R(E_0,E)N_t(E)}{R(E_0,E_0)}, \quad (1)$$

where $N_t(E_0)$ is the number of photons after correction at energy E_0; $N_d(E_0)$ is the number of photons in the measured spectrum at energy E_0; $E_{\max}$ is the maximum energy in the measured spectrum; $R(E_0,E)$ is the monoenergetic response function, which is the proportion of deposited energy in the detector at E when a photon of energy E_0 is received; and $R(E_0,E_0)$ is the full-energy absorption peak efficiency.

The monoenergetic response functions were simulated using GEANT4 (Ref. 36) low energy electromagnetic physics package with photon and electron processes above 250 eV, including photoelectric effect, Compton scattering, Rayleigh scattering, and secondary particles generated after these events. Similar to the work in Ref. 30 and 35, carrier trapping and dead layer of the crystal were not taken into account in the simulation, because they were insignificant in thin (1 mm) CdTe crystals working at high bias voltages.[30] The setup of the simulation is summarized in Table II.

II.D. Comparison of HVL from measurements and from spectra

Half-value layers (HVLs) were calculated from the measured spectra and from TASMIP spectra using the method of Ref. 24 to examine the beam quality of the spectra presented in this work. Filtration of 0.7 mm pure aluminum was applied numerically to the raw spectra before HVL calculation. The mass attenuation coefficients of aluminum and air were obtained from the NIST XCOM database,[37] and the mass energy absorption coefficients of air were obtained by combining the data of NIST XCOM and NIST XAAMDI.[38] Experimental measurements of HVL were also conducted on the

TABLE II. Setup of the Monte Carlo simulation for determining the response function $R(E_0,E)$.

Incident beam	Pencil beam centering at the front of the detector
Interactions	Photoelectronic, Compton, and Rayleigh
Escape events	Fluorescent x-ray generation down to 250 eV
Carrier trapping	Not included
Dead layer	Not included
Photon samples	1×10^6 for each keV
Input x-ray energy	2–125 keV, with 0.5 keV step

Selenia Dimensions system, with the 0.7 mm aluminum and without paddle in the beam. The aluminum sheets used were made of type-1145 aluminum (Fluke Biomedical Al Set, Model 07-434). The reasons to compare HVL of the spectra with 0.7 mm aluminum added filtration were (1) the raw spectra contain large components below 10 keV, which may not be well detected by the ion chamber used in the exposure measurements and (2) the large low energy components also make the calculation of exposure and HVL from the spectra data more prone to errors.

III. RESULTS

III.A. Comparison of selected spectra

The spectra measured with the single-pinhole and double-pinhole configurations, as well the spectra of Boone's TASMIP (Ref. 23) at selected tube voltages (20, 30, 40, and 49 kVp) were compared in Fig. 2.

The spectra in Fig. 2 were corrected with the stripping method described in Sec. II.C and were normalized to their respective total counts for comparison. For 49 kVp which is not covered by the TASMIP mammographic spectral model,[23] only the measured double- and single-pinhole spectra were compared. It should be noted that although x-ray spectra of 43–49 kVp are available in TASMIP general x-ray spectral model,[24] these spectra are much harder than the measured spectra, because they were from a diagnostic x-ray tube with aluminum tube port and additional filtration of 0.5–1.0 mm aluminum were applied in their measurements. For example, the mean energy of the 49-kVp raw spectrum of TASMIP in Ref. 24 is 30.4 keV, while the mean energy of the 49-kVp raw spectrum measured with single pinhole is 17.3 keV.

III.B. Comparison of HVL

HVL obtained from different sources were compared at different kVp in Fig. 3. For the TASMIP spectra, only 20–42

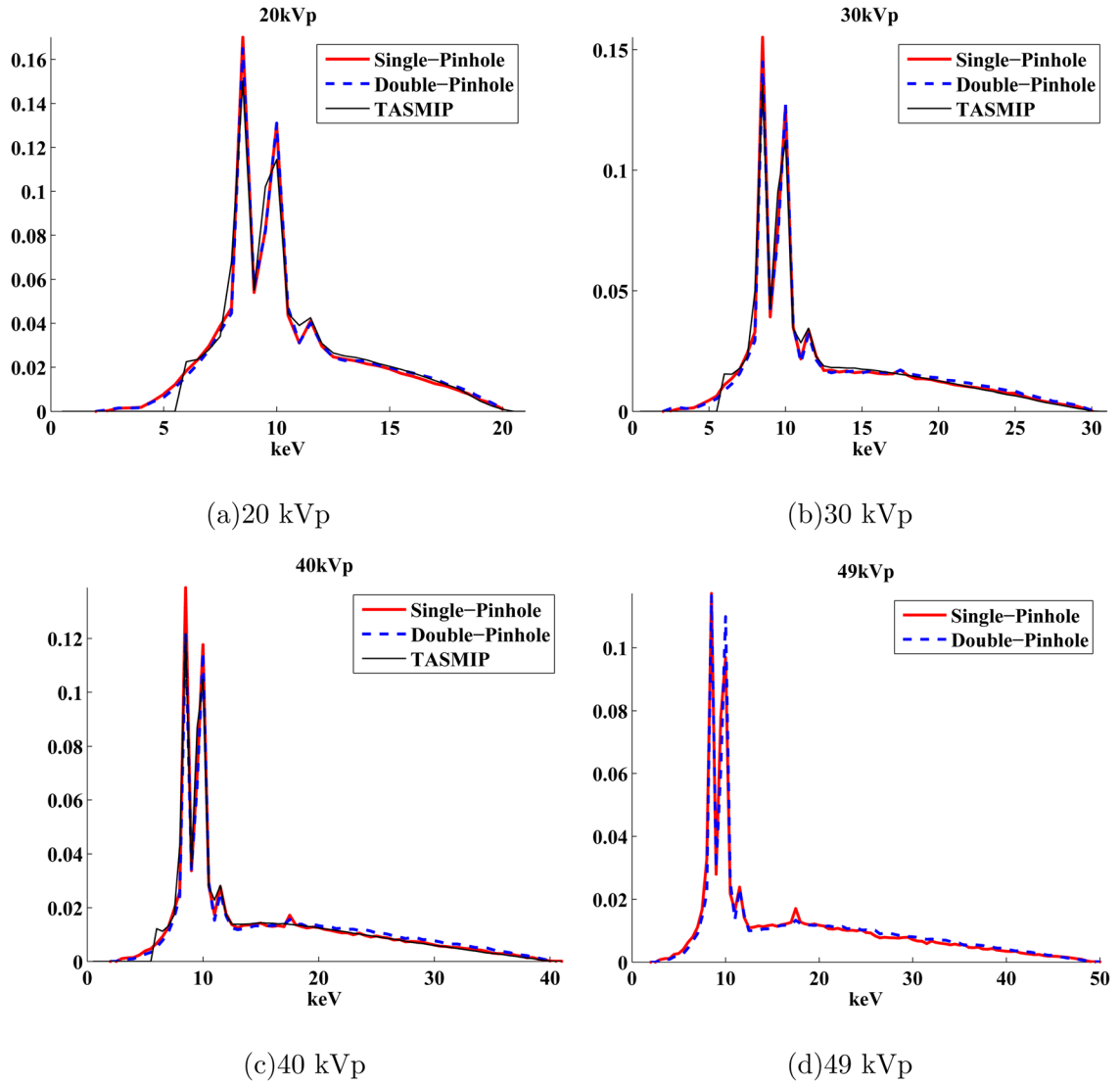

FIG. 2. Comparison of photon number spectra obtained from single-pinhole and double-pinhole setups and from TASMIP model (Ref. 23). Both single- and double-pinhole spectra were corrected for escape events. All spectra were normalized to their own total counts. In (d), the TASMIP spectrum was not shown because the kVp is not covered in TASMIP for mammographic applications.

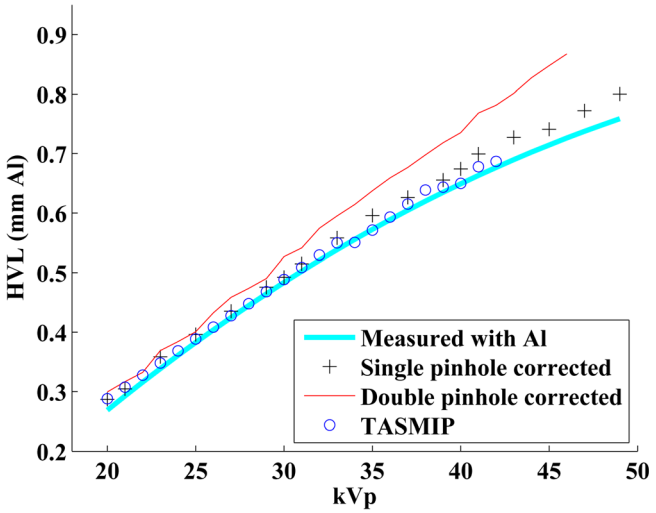

FIG. 3. Comparison of HVL calculated from the spectra and from direct measurements using aluminum foils. Additional filtration of 0.7 mm aluminum was applied to all the raw spectra, and breast paddle was not included.

kVp were covered, as the spectra above 42 kVp in TASMIP (Ref. 24) were too hard—those spectra were from a diagnostic x-ray tube with an aluminum tube port. HVL calculated from the corrected single-pinhole and double-pinhole configurations were presented from 20 to 49 kVp. HVL from the double-pinhole spectra were plotted between 20 and 46 kVp.

III.C. The influence of escape correction

The full-energy absorption peak efficiency $R(E_0, E_0)$ of the spectrometer is shown in Fig. 4, and it is in good agreement with the curve calculated by Miyajima[30] with the LSCAT/EGS4 code, and the one calculated by Bazalova and Verhaegen[35] using EGSnrc/DOSXYZnrc code. The monoenergetic response function $R(E_0, E)$ is also presented in Fig. 5, and the effects of escaped K_α and K_β photons of Cd (23.2 and 26.1 keV) and Te (27.5 and 31 keV) can be seen from the four bright lines to the right of the diagonal [$R(E_0, E_0)$]. Note that Fig. 4 corresponds to the diagonal of Fig. 5.

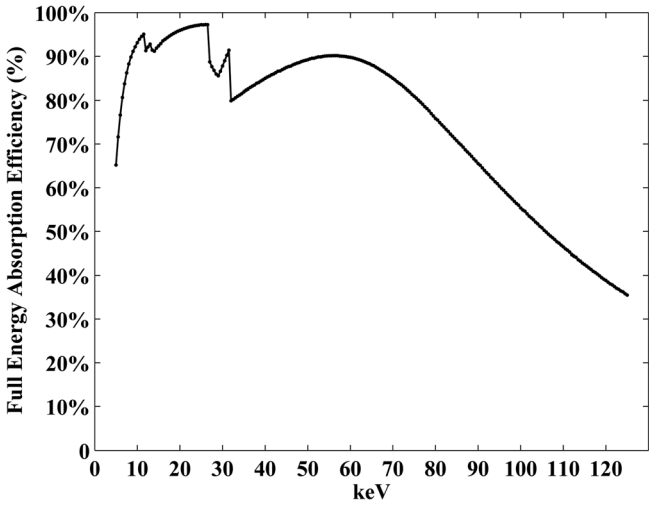

FIG. 4. Full-energy absorption efficiency of the 1 mm thick CdTe detector calculated with GEANT4 Monte Carlo code.

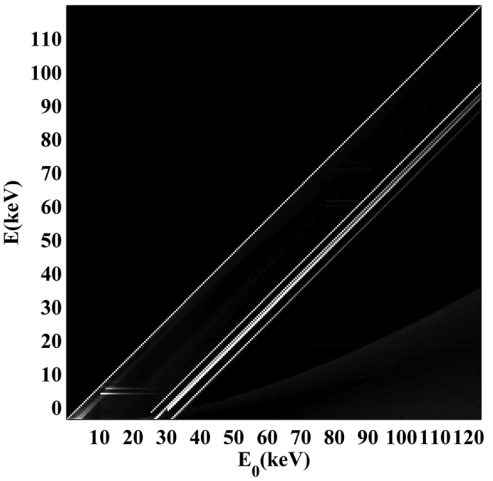

FIG. 5. Monochromatic response function $R(E_0, E)$ of the 1 mm thick CdTe detector calculated with GEANT4 Monte Carlo code.

To study the influence of the escape correction on the spectra, the spectra obtained at 49 kVp using the single-pinhole setup were compared before and after the stripping correction in Fig. 6. The effect of escape correction on the shape of the raw spectrum was small, due to the small portion of high energy components above the K-edges of Cd (26.1 keV) and Te (27.5 keV) in the entire spectra. On the other hand, when the spectra were numerically filtered by 0.7 mm Al, the effect of the escape correction became clearer in Fig. 6: after correction, the spectrum became slightly harder because the heights of energy bins below 26–27 keV were reduced and those above 26–27 keV were increased. This was because the counts contributed by the escape events were removed (stripped) from lower energy bins and were added back to the corresponding high energy bins [Eq. (1)].

To further study the influence of escape correction on spectra of different kVp, photon fluence per exposure (Φ/X) (Refs. 24 and 39) was calculated for each kVp of the single-pinhole and TASMIP mammographic spectra, after being numerically filtered by 0.7 mm aluminum (Fig. 7). Photon

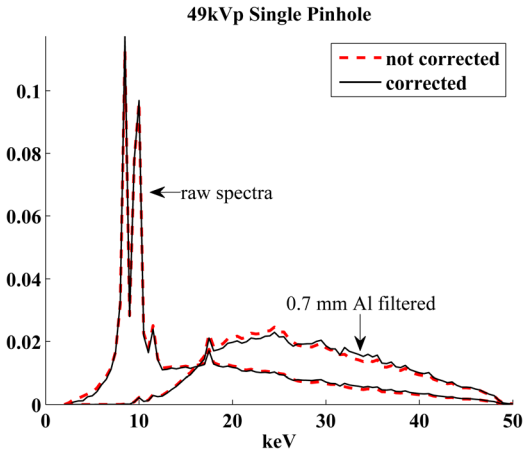

FIG. 6. Spectra with and without the escape correction. The raw spectra were obtained with the single-pinhole setup and were filtered numerically with 0.7 mm Al.

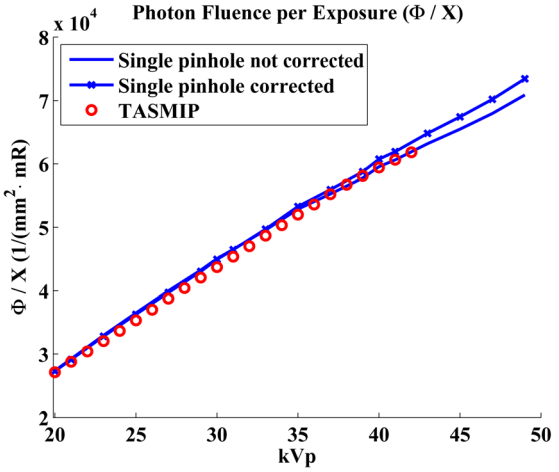

FIG. 7. Photon fluence per exposure calculated from the single-pinhole and TASMIP spectra. All spectra were numerically filtered by 0.7 mm Al.

fluence per exposure is an important quantity in the calculation of detective quantum efficiency,[24] and the details of calculating Φ/X can be found in Ref. 39. Note that the separation between curves of the same collimation setup but with/without escape correction becomes clearer beyond about 35 kVp: the relative difference is less than 0.8% below 35 kVp and is 1.2%–3.6% between 37 and 49 kVp.

IV. DISCUSSION AND CONCLUSION

In this work, we measured the raw x-ray spectra from a Selenia Dimensions DBT system. The new spectral data cover 20–49 kVp, while the existing data of tungsten target for mammographic applications[23] cover 20–42 kVp. The raw spectra measured directly from the tube port without added filtration can be used with numerical filtrations of any material and thickness to match the actual settings of an imaging application and are more flexible than spectra measured with added filtration.

Two configurations for collimating the incident x-ray beam were employed: one with a narrow acceptance aperture achieved with a double-pinhole setup, and the other with a wide acceptance aperture from on single pinhole. We used these configurations to study the difference between the spectra from the focal spot and the spectra from the focal spot and its vicinity. The double-pinhole spectra are generally harder than the single-pinhole ones, as the tail parts toward the maximum kilo-electron-volt of the double-pinhole spectra are higher than those of the single-pinhole ones. In addition, the contribution from the molybdenum anode disk of the target was smaller in the double-pinhole spectra. For example, at 49 kVp [Fig. 2(d)] where the molybdenum peak at 17.5 keV is most significant, the difference of this peak from its neighboring channels is about 0.0044 for the single-pinhole setup, and is 0.0013 for the double-pinhole setup.

Spectral distortions from different sources were considered in this study. From the work of Miyajima,[30] carrier trapping is insignificant for a thin CdTe detector working at high bias voltages. On the other hand, when the range of tube voltage spans to 49 kVp, whether the distortion due to escape events is negligible needs to be studied. In Fig. 4, the full-energy absorption efficiency is between 80% and 89% for 32–49 keV. This means that 11%–20% of the incident photons at these energies will be counted in lower energy channels of the spectra, which necessitates the stripping correction. From Fig. 6, it can be seen that the corrected 49 kVp spectrum begins to be slightly higher than the uncorrected spectrum above 26–27 keV in the raw spectra, and this difference becomes clearer after both spectra were numerically filtered by 0.7 mm Al. Note that 26–27 keV are near Cd's 26.1 keV and Te's 27.5 keV K-edges. The influence of escape correction on spectra of different kVp can be seen in Fig. 7: Φ/X of corrected spectra becomes higher than that of uncorrected spectra beyond about 35 kVp, indicating harder beam quality. This observation is consistent with the finding of Ref. 30 that below 35 kVp the correction of escape events is not necessary.

From Fig. 3, the difference in beam quality of the single-pinhole spectra and double-pinhole spectra can be observed more easily. The HVL obtained with the double-pinhole spectra is higher (e.g., 0.04–0.1 mm aluminum higher starting from 31 kVp) than that of single-pinhole spectra at each kVp. The differences between the HVL of the double-pinhole spectra and the measured HVL are at most 0.14 mm Al, while the HVL of the single-pinhole spectra agreed with the measured HVL within 0.04 mm Al. It should be noted that the HVL calculated in this study was based on mass attenuation coefficients of pure aluminum, while in the actual HVL measurements type-1145 aluminum sheets were used (consisting of $>99.45\%$ aluminum and other elements of higher atomic numbers, e.g., Si and Fe), which could cause smaller HVL measurements than if pure aluminum sheets had been used. The reason for using the attenuation coefficients of pure Al instead of type-1145 aluminum was that the vendor only specified ranges of percentage elemental composition of the alloy, and the exact composition of the alloy may differ from batch to batch. The HVL calculated using the corrected single-pinhole setup agreed with those calculated with the TASMIP spectra within 0.025 mm Al. In addition, the curves of photon fluence per exposure also showed good agreement in Fig. 7. For the double-pinhole spectra, we observed a drop of HVL values from 46 kVp (0.87 mm Al) to 47 kVp (0.84 mm Al) and 48 kVp (0.85 mm Al). This drop might be attributed to that the double-pinhole setup (due to its small acceptance aperture) was sensitive to the position of the focal spot which might have slight shift after many exposures in the experiment or at the high end of the kVp range.

The difference between the double- and single-pinhole measurements lies in the fact that the double-pinhole has a much smaller acceptance aperture (diameter of 2 mm projected on the plane of the focal spot, see Sec. II.B) and what it measures are photons from the close vicinity of the focal spot. On the other hand, the single-pinhole method has a much larger acceptance aperture and it receives not only primary photons but also off-focus radiation.[26] In fact, the ion chamber used in the HVL measurements also has a large acceptance aperture

and that should be the reason why the measured HVL agreed better with the single-pinhole spectra. For clinical purpose, both the imaging subject and individual detector pixels have large acceptance apertures, and the x-ray spectra they receive should be close to the single-pinhole measurements.

In this work, we presented the new spectral measurements on a Selenia Dimensions system, which has a tungsten target and operates at 20–49 kVp. Despite the experimental difficulty and complexity, the spectra from the single-pinhole setup showed good agreement with the existing TASMIP mammographic spectra, and its beam quality is consistent with the experimentally measured HVL. The comparison between the spectra from the single-pinhole and double-pinhole setup revealed the difference between spectra from the focal spot and spectra from focal spot and its vicinity, which is of interest for future investigations on the impact to image quality and patient dose. The new data and observations in this study should be useful for future research based on DBT systems.

ACKNOWLEDGMENTS

The authors want to thank Dr. Baorui Ren of Hologic for kindly providing the device and critical support for the experiments and would like to acknowledge Amptek for offering the spectrometer and technical support. This work used the High Performance Clusters of the Partners Cooperation for Monte Carlo calculations, and the authors thank the Enterprise Research IS group at Partners Healthcare for their in-depth support.

[a]Author to whom correspondence should be addressed. Electronic mail: bliu7@bics.bwh.harvard.edu

[1]A. Karellas and S. Vedantham, "Breast cancer imaging: A perspective for the next decade," Med. Phys. **35**, 4878–4897 (2008).
[2]G. Ullman, M. Sandborg, D. R. Dance, M. Yaffe, and G. A. Carlsson, "A search for optimal x-ray spectra in iodine contrast media mammography," Phys. Med. Biol. **50**, 3143–3152 (2005).
[3]P. Bernhardt, T. Mertelmeier, and M. Hoheisel, "X-ray spectrum optimization of full-field digital mammography: Simulation and phantom study," Med. Phys. **33**, 4337–4349 (2006).
[4]N. T. Ranger, J. Y. Lo, and E. Samei, "A technique optimization protocol and the potential for dose reduction in digital mammography," Med. Phys. **37**, 962–969 (2010).
[5]A.-K. Carton, C. Ullberg, K. Lindman, R. Acciavatti, T. Francke, and A. D. A. Maidment, "Optimization of a dual-energy contrast-enhanced technique for a photon-counting digital breast tomosynthesis system: I. A theoretical model," Med. Phys. **37**, 5896–5907 (2010).
[6]A.-K. Carton, C. Ullberg, and A. D. A. Maidment, "Optimization of a dual-energy contrast-enhanced technique for a photon-counting digital breast tomosynthesis system: II. An experimental validation," Med. Phys. **37**, 5908–5913 (2010).
[7]E. Samei and R. S. Saunders, Jr., "Dual-energy contrast-enhanced breast tomosynthesis: Optimization of beam quality for dose and image quality," Phys. Med. Biol. **56**, 6359–6378 (2011).
[8]S. Vedantham, A. Karellas, and S. Suryanarayanan, "Attenuation characteristics of fiberoptic plates for digital mammography and other x-ray imaging applications," J. X-Ray Sci. Technol. **11**, 219–230 (2003).
[9]J. Robert S. Saunders, E. Samei, J. L. Jesneck, and J. Y. Lo, "Physical characterization of a prototype selenium-based full field digital mammography detector," Med. Phys. **32**, 588–599 (2005).
[10]B. Lazzari, G. Belli, C. Gori, and M. R. D. Turco, "Physical characteristics of five clinical systems for digital mammography," Med. Phys. **34**, 2730–2743 (2007).
[11]G. Richard Hammerstein, D. W. Miller, D. R. White, M. Ellen Masterson, H. Q. Woodard, and J. S. Laughlin, "Absorbed radiation dose in mammography," Radiology **130**, 485–491 (1979), http://radiology.rsna.org/content/130/2/485.full.pdf+html.
[12]X. Wu, G. T. Barnes, and D. M. Tucker, "Spectral dependence of glandular tissue dose in screen-film mammography," Radiology **179**, 143–148 (1991).
[13]J. M. Boone, "Glandular breast dose for monoenergetic and high-energy x-ray beams: Monte Carlo assessment," Radiology **213**, 23–37 (1999).
[14]J. M. Boone, "Normalized glandular dose (DgN) coefficients for arbitrary x-ray spectra in mammography: Computer-fit values of Monte Carlo derived data," Med. Phys. **29**, 869–875 (2002).
[15]I. Sechopoulos, S. Suryanarayanan, S. Vedantham, C. D'Orsi, and A. Karellas, "Computation of the glandular radiation dose in digital tomosynthesis of the breast," Med. Phys. **34**, 221–232 (2007).
[16]D. R. Dance, K. C. Young, and R. E. van Engen, "Estimation of mean glandular dose for breast tomosynthesis: Factors for use with the UK, European and IAEA breast dosimetry protocols," Phys. Med. Biol. **56**, 453–471 (2011).
[17]J. Kaufhold, J. A. Thomas, J. W. Eberhard, C. E. Galbo, and D. E. G. Trotter, "A calibration approach to glandular tissue composition estimation in digital mammography," Med. Phys. **29**, 1867–1880 (2002).
[18]M. Yaffe, "Mammographic density. Measurement of mammographic density," Breast Cancer Res. **10**, 209 (2008).
[19]J. L. Ducote and S. Molloi, "Quantification of breast density with dual energy mammography: An experimental feasibility study," Med. Phys. **37**, 793–801 (2010).
[20]J. M. Lewin and L. Niklason, "Advanced applications of digital mammography: Tomosynthesis and contrast-enhanced digital mammography," Semin. Roentgenol. **42**, 243–252 (2007).
[21]S. C. Kappadath and C. C. Shaw, "Quantitative evaluation of dual-energy digital mammography for calcification imaging," Phys. Med. Biol. **49**, 2563–2576 (2004).
[22]A. D. Laidevant, S. Malkov, C. I. Flowers, K. Kerlikowske, and J. A. Shepherd, "Compositional breast imaging using a dual-energy mammography protocol," Med. Phys. **37**, 164–174 (2010).
[23]J. M. Boone, T. R. Fewell, and R. J. Jennings, "Molybdenum, rhodium, and tungsten anode spectral models using interpolating polynomials with application to mammography," Med. Phys. **24**, 1863–1874 (1997).
[24]J. M. Boone and J. A. Seibert, "An accurate method for computer-generating tungsten anode x-ray spectra from 30 to 140 kv," Med. Phys. **24**, 1661–1670 (1997).
[25]T. R. Fewell and R. E. Shuping, *Handbook of Mammographic X-Ray Spectra* (HEW, Rockville, MD, 1978).
[26]J. T. Bushberg, J. A. Seibert, E. M. Leidholdt, Jr., and J. M. Boone, The Essential Physics of Medical Imaging, 2nd ed. (Lippincott Williams and Wilkins, Philadelphia, 2002), pp. 97–144.
[27]B. Ren, C. Ruth, J. Stein, A. Smith, I. Shaw, and Z. Jing, "Design and performance of the prototype full field breast tomosynthesis system with selenium based flat panel detector," Proc. SPIE **5745**, 550–561 (2005).
[28]S. Miyajima, K. Imagawa, and M. Matsumoto, "CdZnTe detector in diagnostic x-ray spectroscopy," Med. Phys. **29**, 1421–1429 (2002).
[29]S. Miyajima and K. Imagawa, "CdZnTe detector in mammographic x-ray spectroscopy," Phys. Med. Biol. **47**, 3959–3972 (2002).
[30]S. Miyajima, "Thin CdTe detector in diagnostic x-ray spectroscopy," Med. Phys. **30**, 771–777 (2003).
[31]E. D. Castro, R. Pani, R. Pellegrini, and C. Bacci, "The use of cadmium telluride detectors for the qualitative analysis of diagnostic x-ray spectra," Phys. Med. Biol. **29**, 1117–11131 (1984).
[32]K. Maeda, M. Matsumoto, and A. Taniguchi, "Compton-scattering measurement of diagnostic x-ray spectrum using high-resolution schottky cdte detector," Med. Phys. **32**, 1542–1547 (2005).
[33]R. Redus, J. Pantazis, T. Pantazis, A. Huber, and B. Cross, "Characterization of CdTe detectors for quantitative x-ray spectroscopy," IEEE Trans. Nucl. Sci. **56**, 2524–2532 (2009).
[34]*Handbook of X-Ray Spectrometry*, 2nd ed., edited by R. E. V. Grieken and A. A. Markowicz (Marcel Dekker, Inc., New York, NY, 2002).
[35]M. Bazalova and F. Verhaegen, "Monte Carlo simulation of a computed tomography x-ray tube," Phys. Med. Biol. **52**, 5945–5955 (2007).
[36]S. Agostinelli *et al.*, "GEANT4–A simulation toolkit," Nucl. Instrum. Methods Phys. Res. A **506**, 250–303 (2003).
[37]M. Berger, J. Hubbell, S. Seltzer, J. Chang, J. Coursey, R. Sukumar, D. Zucker, and K. Olsen, "XCOM: Photon Cross Sections Database,"

Radiation and Biomolecular Physics Division, PML, National Institute of Standards and Technology (available URL: http://www.nist.gov/pml/data/xcom/index.cfm). Last accessed December 9, 2011.
[38]J. H. Hubbell and S. M. Seltzer, *Tables of X-Ray Mass Attenuation Coefficients and Mass Energy-Absorption Coefficients from 1 keV to 20 MeV for Elements Z = 1 to 92 and 48 Additional Substances of Dosimetric Interest* (National Institute of Standards and Technology, http://www.nist.gov/pml/data/xraycoef/index.cfm, 2004).
[39]D. Zhang, X. Wu, M. Wong, Y. Ni, J. Rong, W. R. Chen, and H. Liu, "Error analysis in the measurement of x-ray photon fluence: An analysis on the uncertainty from energy calibration," Proc. SPIE **7176**, 71760I (2009).
[40]See supplementary material at http://dx.doi.org/10.1118/1.4719958 for the spectral data measured with the single- and double-pinhole configurations described in this paper. For more information on supplementary material, see http://www.aip.org/pubservs/epaps.html.